



Deposited via The University of Leeds.

White Rose Research Online URL for this paper:

<https://eprints.whiterose.ac.uk/id/eprint/227913/>

Version: Accepted Version

Article:

Lyu, P., Luo, Q., Wang, T. et al. (2025) Serviceability of railway slab track foundations with retaining walls under train loading. *International Journal of Rail Transportation*, 13 (1). pp. 23-48. ISSN: 2324-8378

<https://doi.org/10.1080/23248378.2024.2326514>

This item is protected by copyright. This is an author produced version of an article published in the *International Journal of Rail Transportation*. Uploaded in accordance with the publisher's self-archiving policy.

Reuse

Items deposited in White Rose Research Online are protected by copyright, with all rights reserved unless indicated otherwise. They may be downloaded and/or printed for private study, or other acts as permitted by national copyright laws. The publisher or other rights holders may allow further reproduction and re-use of the full text version. This is indicated by the licence information on the White Rose Research Online record for the item.

Takedown

If you consider content in White Rose Research Online to be in breach of UK law, please notify us by emailing eprints@whiterose.ac.uk including the URL of the record and the reason for the withdrawal request.

Serviceability of railway slab track foundations with retaining walls under train loading

Pengju Lyu

School of Civil Engineering, Southwest Jiaotong Univ., Chengdu 610031, China

Qiang Luo

School of Civil Engineering, Southwest Jiaotong Univ., Chengdu 610031, China;

MOE Key Laboratory of High-speed Railway Engineering, Southwest Jiaotong Univ., Chengdu 610031, China

Tengfei Wang*

School of Civil Engineering, Southwest Jiaotong Univ., Chengdu 610031, China;

MOE Key Laboratory of High-speed Railway Engineering, Southwest Jiaotong Univ., Chengdu 610031, China

E-mail: w@swjtu.edu.cn; ORCID: 0000-0003-4079-0687 (*Corresponding author)

David P. Connolly

School of Civil Engineering, University of Leeds, Leeds LS2 9JT, UK

Email: D.Connolly@leeds.ac.uk

Qingzhi Ye

School of Civil Engineering, Southwest Jiaotong Univ., Chengdu 610031, China

1 **Abstract**

2 Railway retaining wall designs tend to disregard vehicle-induced trackbed deformation control, despite
3 its potential impact on infrastructure serviceability. To fill this gap, this study seeks to develop an
4 improved method to assess the performance of railway gravity retaining walls, specifically focusing
5 on managing slab trackbed deformation. Utilizing a validated 3D numerical model, the research
6 examines the impact of five parameters—wall width, location, inclination, embankment height, and
7 ground bearing capacity—on trackbed surface displacement (ω) arising from train loading. The
8 multivariate adaptive regression splines (MARS) approach is applied to establish the mathematical
9 relationship between these factors and an assessment indicator for evaluating track foundation
10 serviceability. This indicator is the trackbed surface displacement index (R_ω), signifying the ratio of
11 the maximum allowable to the practical ω value. Results highlight the necessity for comprehensive
12 retaining wall design to ensure $R_\omega \geq 1.0$, particularly when the wall is near the track, steeply inclined,
13 or supporting a tall embankment.

14 *Keywords:* Gravity retaining wall; track foundation; trackbed surface displacement; train loading;
15 multivariate adaptive regression splines

16

Nomenclature

BFs	Basis functions	$(\gamma_d)_t$, $(\gamma_d)_{K30}$	The shear strain of soil in working condition and in K_{30} test
FDM	Finite difference method	γ_r	The reference shear strain
GCV	Generalized cross-validation	γ_{tv} , $\gamma_{tv,M}$	A threshold and the mean value of threshold for γ_d
MAE	Mean absolute error	h	Height of a low slope above the wall top
MARS	Multivariate adaptive regression splines	h_1	Height of wall toe step
RMSE	Root mean square error	H , H_e	Height of wall and embankment
α	Inclination angle of wall back	I	Predefined maximum number of BFs
α_o	Wall base angle with respect to the horizontal plane	I_p	The plasticity index of soil
b , $[b]$, $[b_\omega]$	Wall width and its minimum value for stability requirements, as well as minimum value corresponding to $[\omega]$	K_{30}	Modulus of subgrade reaction
b_1	Width of wall toe step	$K_{h,0}$	Coefficient of earth pressure at rest
b_{max} , b_{min}	Maximum and minimum wall width	L	Number of observations in MARS model
b_t	Width of track structure	$\lambda_i(X)$	The i^{th} basis function
B	Width of wall base	μ	Poisson's ratio
β	The ratio of R_t to R_{K30}	$1:n$	Slope of wall face
β_0 , β_i	Constant term and the i^{th} basis function's coefficient in MARS model	ω , $[\omega]$	Trackbed surface displacement due to train loading and its maximum allowable value
d , d_s	Horizontal distance from centreline of the track to edge of the embankment shoulder and vertex of wall back	ω_r , ω_f	Value of ω with a fully restrained wall and increment of ω caused by wall movement
d_h	Buried depth of retaining wall	p	Average applied pressure in K_{30} test
d_{K30}	Diameter of loading plate in K_{30} test	P_0 , P_d	Static axle load and axle load applied on rail
D	Line spacing for a double-track	R^2	Coefficient of determination
Δ_m	Horizontal displacement of the wall induced by the train loading at half height	R_b	Ratio of $[b_\omega]$ to $[b]$
E , E_e	Deformation modulus and elastic modulus	R_t , R_{K30}	Modulus ratio for working condition and K_{30} test condition
$[\varepsilon_{11}]$, $(\varepsilon_d)_{K30}$	The threshold for rapid convergence of soil compression strain and the average compressive strain in the K_{30} test	R_ω	Ratio of $[\omega]$ to ω
$f(X)$, $f(X_l)$	Output variable and the l^{th} observation predicted by MARS model	R_ω	MARS predicted value of R_ω
φ , φ_l	Friction angle of soil and interface	s	The settlement observed in K_{30} test
Φ_{kl}	Dynamic amplification factor	σ_0	Ground bearing capacity
g	Penalizing parameter	$\tan\alpha$	Tangent value of α
G_d , G_{max}	The dynamic shear modulus and its maximum value	y_l	Actual value of the l^{th} observation
γ_d	Shear strain of soil		

19 **1. Introduction**

20 The primary function of a retaining wall is to provide support to a vertical or nearly vertical
21 geotechnical surface, thereby preventing potential collapse. In addition, retaining walls offer a
22 reduction in footprint when compared to slopes. Gravity retaining walls, commonly constructed from
23 materials like masonry or concrete, rely on their self-weight to counteract earth pressure [1]. These
24 walls are widely used in infrastructure projects, such as roads and railways, due to their simple
25 construction and ease of installation [2–5]. Numerical simulations [6–8], model tests [2,9], analytical
26 methods [5,10–16], and field tests [17,18] are widely employed in studying this classical wall type.
27 However, in the collected data, researchers have extensively focused on stability analysis [5,15,16,19],
28 meaning earth pressure calculations have received significant attention. Besides the classic Rankine
29 and Coulomb theories, various methods for earth pressure calculation have been developed [10–14].
30 However, the stability check for gravity retaining walls aims only to ensure that the geotechnical
31 structure remains undamaged, without accounting for backfill deformation.

32 Xie and Luo [20] and Wang and Xiao [21] have emphasized the intricate relationship between the
33 displacement of a retaining wall and the deformation of the adjacent soil. Additionally, centrifugal
34 model tests [22] have demonstrated that greater displacement of the wall can result in more substantial
35 surface settlement of the fill behind it. It is conceivable that insufficient support capacity of the gravity
36 retaining wall, which sustains the railway track foundation, could lead to excessive wall displacement
37 and subsequent deformation of the retained fill. Therefore, considering the deformation of the fill
38 behind the wall during the performance check at the design stage is crucial.

39 Slab track [23–26], as compared to ballasted track [27–29], demands less maintenance and is

40 prevalently utilized in high-speed railway projects. Its concrete slab structures exhibit considerable
41 rigidity, which leads to minimal deformation under the passing trains. This rigidity ensures a stable
42 and smooth rail surface. However, the significant rigidity of slab track presents challenges in adapting
43 to foundation deformation [30]. The lack of adaptability between the track and foundation increases
44 the propensity for cracks in the concrete track components and exacerbates the cumulative deformation
45 of the foundation [23]. This concern is one of the reasons for stringent requirements for foundation
46 settlement in high-speed railways [31,32]. Consequently, managing foundation deformation is critical,
47 especially for slab track foundation supported by gravity retaining walls.

48 The trackbed, the top layer of the track foundation, connects the track structure to the subgrade.
49 The displacement of the trackbed surface caused by train loading has a direct impact on the train
50 operation [33] and can serve as an evaluation indicator of the retaining wall's impact on soil
51 deformation. Therefore, examining the relationship between gravity retaining wall design parameters
52 and trackbed surface displacement is essential for assessing the wall's role in controlling track
53 foundation deformation. However, this aspect is often overlooked in the design of railway retaining
54 structures.

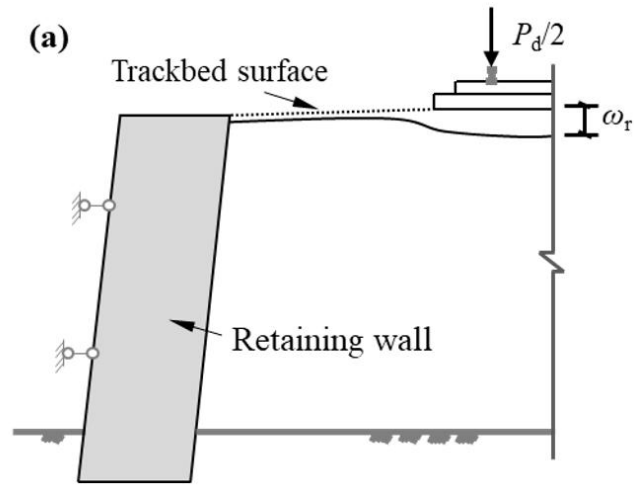
55 This study endeavors to bridge the gap in knowledge by presenting a three-dimensional numerical
56 models of slab track foundation supported by gravity retaining wall with a landward-leaning back [34].
57 These numerical models were developed and solved using the commercial software Fast Lagrangian
58 Analysis of Continua (FLAC^{3D}) [35]. The initial phase of the study involved an examination of the
59 train-induced trackbed surface displacement's distribution characteristics, influenced by five wall-
60 associated variables: width, position, inclination, embankment height, and ground bearing capacity.

61 Following this, a methodological framework employing multivariate adaptive regression splines
62 (MARS) [36] was applied to establish a correlative mapping between factors and the trackbed surface
63 displacement. Utilizing the MARS-based model, the subsequent analysis established the necessary
64 wall width to ensure trackbed surface displacement remains within acceptable thresholds. This width
65 was then contrasted with design results derived from traditional recommended methods. The
66 conclusions drawn from this study provide insights to the design and construction of gravity retaining
67 walls supporting slab track foundations.

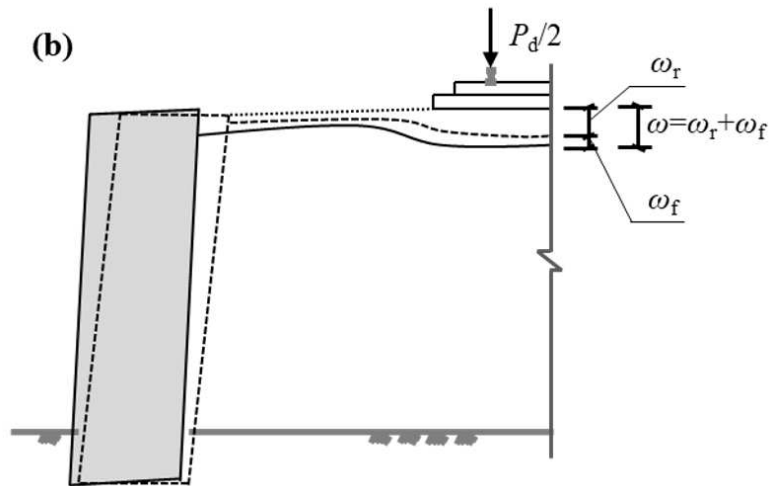
68 **2. Numerical model**

69 This section introduces a 3D numerical model of a retaining wall-supported foundation, solved using
70 the finite difference method (FDM). The model aims to investigate the relationship between the railway
71 retaining wall and the trackbed surface displacement (ω) induced by train loading. ω comprises two
72 primary components: displacement ω_r with a fully restrained wall prior to any settlement, and
73 displacement ω_f following the wall movement, as depicted in Figure 1. Specifically, when the retaining
74 wall is motionless, as shown in Figure 1a, the vertical displacement of the trackbed surface caused by
75 the train's axle loading (P_d) is ω_r . However, the retaining wall also moves due to the additional earth
76 pressure under train loading, resulting in an additional displacement ω_f on the trackbed surface, as
77 shown in Figure 1b. Thus, it can be inferred that the total trackbed settlement is the combination of
78 track-loading induced (no wall movement) and retaining wall displacement induced: $\omega = \omega_r + \omega_f$.
79 Distinguishing these components in practical engineering scenarios is challenging. The analysis of ω_r
80 focuses on investigating the deformation of the track foundation when an existing retaining wall
81 undergoes subsequent reinforcement. In contrast, ω_f highlights the variation of track foundation

82 deformation between conditions before and after additional wall movement.



83



84

85 **Figure 1.** Components of trackbed surface displacement under train loading: (a) motionless wall; (b) wall movement
86 present.

87 **2.1. Track-foundation model**

88 Figure 2 depicts a cross-sectional view of a railway foundation with a landward-leaning retaining wall.

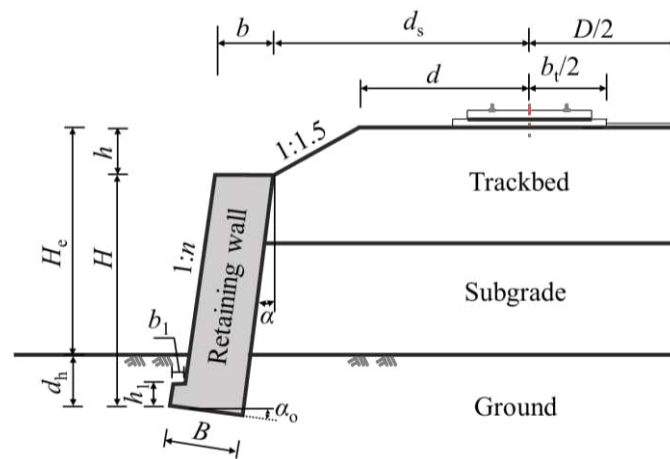
89 The structure includes, from top to bottom: the track, the embankment with retaining wall, and the

90 ground. The embankment, having a height of H_e , consists of a trackbed and a subgrade underneath the

91 trackbed. The gravity retaining wall possesses a height of H , a top width of b , and a buried depth of d_h .

92 It features a wall face slope of 1: n , a wall inclination angle of α , and a base width of B positioned at

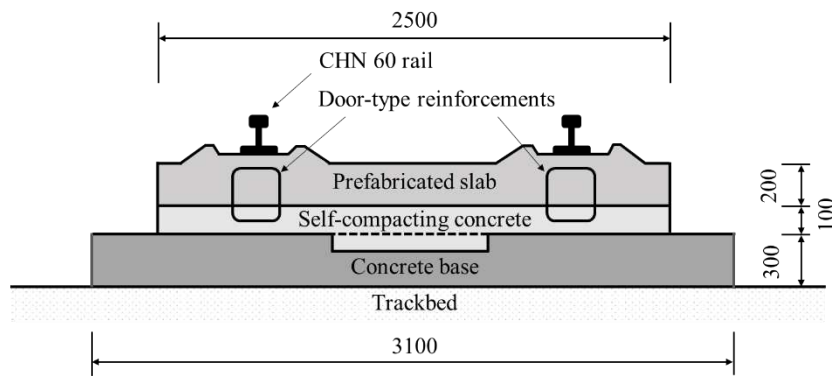
93 an angle α_o with respect to the horizontal plane. The wall toe step has a height of h_1 and a breadth of
 94 b_1 . The wall's location is determined by the distance d_s between the centreline of the track adjacent to
 95 the wall and the highest point at the wall back. Additionally, there is a low slope above the top of the
 96 wall, having a height of h and a gradient of 1:1.5. Finally, the track structure is situated on the trackbed
 97 surface, encompassing a width of b_t , a distance of d from the edge of the embankment shoulder, and a
 98 line spacing D to a neighbouring track. Notably, in engineering practice, the inclination angle (α) of a
 99 landward-leaning wall back is conventionally expressed as a negative value, where a smaller absolute
 100 value indicates increased steepness of the wall.



101
 102 **Figure 2.** Cross section of the track structure and substructure.

103 A 3D numerical finite difference model is introduced to examine the correlation between the quasi-
 104 static displacement of the trackbed surface due to train loading and the retaining wall. The wall's
 105 geometric parameters, location, and ground bearing capacity are analysed to assess their impact. The
 106 slab track structure (Figure 3) consists of CHN 60 rails, fasteners, prefabricated concrete slab, self-
 107 compacting concrete layers, and concrete bases [30,37]. The rails are attached to the prefabricated
 108 slabs using fasteners, while the reinforcements and protruding columns link the prefabricated slabs,

109 self-compacting concrete layers, and bases sequentially. The CHN 60 rail features a cross-sectional
 110 area of 77.45 cm^2 , a moment of inertia of $3,217 \text{ cm}^4$ about the horizontal axis, and 524 cm^4 about the
 111 vertical axis. WJ-8B fasteners with a longitudinal spacing of 0.63 m and a vertical dynamic stiffness
 112 of 50 kN/mm [30] are utilized. The prefabricated track slab and self-compacting concrete layer possess
 113 widths of 2.5 m and thicknesses of 0.2 m and 0.1 m, respectively. The base slab has a width (b_t) of 3.1
 114 m and a thickness of 0.3 m.

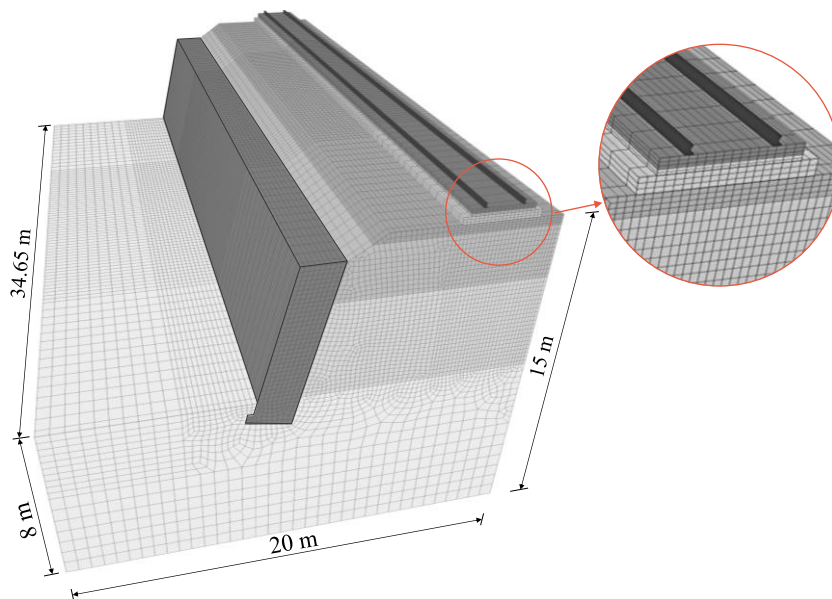


115
 116 **Figure 3.** Illustration of the slab track (unit: mm).

117 The general embankment has a cross-section of $d = 4.3 \text{ m}$, $D = 5 \text{ m}$, and a slope of 1:1.5. When
 118 supported by a gravity retaining wall, the height of the wall is calculated as $H = H_e + d_h - h$, where h
 119 can be determined by $h = (d_s - 4.3 \text{ m})/1.5$ for $d_s > 4.3 \text{ m}$ and $h = 0$ for $d_s \leq 4.3 \text{ m}$. The trackbed has a
 120 thickness of 2.7 m. In numerical model, the retaining wall has $d_h = 1.0 \text{ m}$, $b_1 = 0.25 \text{ m}$, $h_1 = 0.4 \text{ m}$, and
 121 $\tan\alpha_o = 0.2$. The ground has a width of 20 m and a depth of 8.0 m.

122 Field tests indicate that the stress exerted on a trackbed surface of ballastless railway by an
 123 individual bogie is distributed longitudinally over a length of approximately 8 to 10 m [25]. To
 124 minimize boundary condition impacts, the FDM model's longitudinal dimension is 34.65 m, equivalent
 125 to 55 fastener spacings. Beam structural elements simulate the steel rails, while solid elements

126 represent most other structural components. Springs simulate fasteners at the contact nodes between
127 the rail and the prefabricated track slab. The prefabricated track slab and self-compacting concrete
128 share common gridpoints at their contact positions to prevent relative displacement between layers.
129 Interface elements with friction coefficients of 0.7 [25] and 0.5 [30] are used to simulate the interaction
130 between the concrete base and self-compacting concrete, as well as the trackbed. Additionally, the
131 interfaces between the trackbed, subgrade, and ground are fixed in contact. Furthermore, interface
132 elements determine the wall-soil interaction. The FDM model, illustrated in Figure 4, is composed of
133 258,710 elements and 279,212 gridpoints. The vertical outer surfaces are subject to limitations on
134 normal displacement (i.e. roller boundaries). Similarly, the bottom of the model is restricted for both
135 perpendicular and parallel displacements (i.e. pinned boundaries).



136
137 **Figure 4.** Configuration and meshes of the track-foundation FDM model.

138 The numerical simulation, considering the construction process, is divided into the following steps:

- 139 **a)** Determine the geostatic stress field of the ground;
- 140 **b)** Apply gravitational loads to the retaining wall and embankment fill and determine the stress

141 distribution due to self-weight;

142 c) Determine the stress field in response to the gravity of the track by activating the track structure;

143 d) Restrict the displacement of the retaining wall and place dual-axle loads on the rail. Loading is
144 positioned at the centre in the longitudinal direction of the model to derive the value of ω_r .

145 e) Compute the value of ω by removing the restriction on the retaining wall. Then, determine ω_f
146 as ω minus ω_r .

147 The deformation within track foundation under train loading is primarily contributed by the
148 deformation of trackbed [38]. Hence, the soil deformation beneath the trackbed is excluded from the
149 calculations of ω_r and ω . The axle load of the bogie, denoted as P_d , is calculated using the formula P_d
150 $= \Phi_{kl} \cdot P_0$, where P_0 , representing the static axle load, is 170 kN, and the axle spacing is 2.5 m. The
151 effect of track irregularity is incorporated by employing the amplification factor, Φ_{kl} , which augments
152 static loading. Φ_{kl} is established at 1.20, based on test data collected from the Wuhan-Guangzhou high-
153 speed railway [39]. This value corresponds to a train speed of 250 km/h with considering average track
154 irregularity and a coverage probability of 75%, as determined by simulation methods [24].

155 **2.2. Material properties and interface**

156 The concrete used for both the slab track and the retaining wall is modelled as linearly elastic material.

157 The soil is simulated using an elastoplastic model with the Mohr-Coulomb failure criterion. The
158 material parameters are listed in Table 1. Additionally, this subsection outlines the methodology for
159 using the modulus of subgrade reaction (K_{30}) to estimate the soil modulus. Subsequently, it outlines
160 the process for determining other ground parameters using ground bearing capacity (σ_0), a primary
161 metric for characterizing ground performance in design. The subsection concludes with a presentation

162 of interface model.

163 **Table 1.** Material properties.

Component	Material	Density (kg·m ⁻³)	Deformation modulus E (MPa)	Elastic modulus E_e (MPa)	Poisson's ratio μ	Friction angle φ (°)	Dilation angle (°)
Retaining wall	C30 concrete	2,300	—	30,000	0.20	—	—
Rail	Steel	7,830	—	210,000	0.30	—	—
Prefabricated slab	C60 concrete	2,500	—	36,000	0.20	—	—
Self-compacting concrete	C40 concrete	2,500	—	32,500	0.20	—	—
Concrete base	C40 concrete	2,500	—	32,500	0.20	—	—
Upper trackbed	Graded gravel	2,100	41.9	214.0	0.25	41.8	0.5φ
Lower trackbed	Coarse fill	2,050	32.1	168.6	0.30	35.0	0.5φ
Subgrade	Coarse fill	2,000	27.9	147.8	0.30	34.5	0.5φ
Ground	Coarse- grained soil	1,900			*		0.5φ

164 **Note:** *The values of variables are estimated based on the ground bearing capacity σ_0 .

165 2.2.1. Soil modulus

166 The ability of foundation soil to resist applied forces and subsequent deformation is primarily
 167 influenced by its modulus, which considers loading characteristics. For evaluating the influence of
 168 self-weight loading, the deformation modulus (E) is employed. Conversely, the elastic modulus (E_e) is
 169 pertinent for assessing the effects of train loading. Luo et al. [40] suggest K_{30} can be used to estimate
 170 both E and E_e . Under the assumption of elasticity, the average applied pressure (p) and the settlement
 171 (s) observed in K_{30} test can be described by Equation (1) [41]:

$$172 \quad s = 0.785(1 - \mu^2)d_{K30}p/E \quad (1)$$

173 where μ represents the Poisson's ratio of soil, and d_{K30} denotes the diameter of the circular loading
 174 plate. By setting d_{K30} to 0.3 m and s to 1.25 mm, it can be obtained that the ratio of p/s is the value of
 175 K_{30} . Subsequently, Equation (2) can be derived to estimate E , utilizing the K_{30} value.

$$176 \quad E = 0.785(1 - \mu^2)d_{K30}K_{30} \quad (2)$$

177 The relationship between E_e and E is defined by Equation (3) [40]:

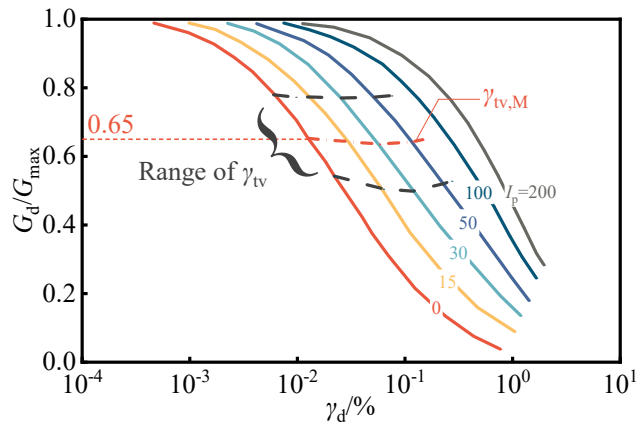
178
$$E_e = \beta E \quad (3)$$

179 where β is defined as the ratio of the shear modulus ratio R_t , which corresponds to the strain conditions
 180 experienced by the track foundation fill under train loading, to the modulus ratio R_{K30} observed at the
 181 K_{30} test, as determined by Equation (4) [40,42]:

182
$$\beta = \frac{R_t}{R_{K30}} = \frac{1/(1+(\gamma_d)_t/\gamma_r)}{1/(1+(\gamma_d)_{K30}/\gamma_r)} \quad (4)$$

183 where γ_r represents the reference shear strain. $(\gamma_d)_{K30}$ denotes the shear strain observed under the K_{30}
 184 test condition. Meanwhile, $(\gamma_d)_t$ refers to the shear strain experienced in the working state when
 185 subjected to train loading.

186 Figure 5 illustrates the correlation curve between shear modulus reduction (G_d/G_{max}) and shear
 187 strain (γ_d) of the soil [40,43], where G_d and G_{max} are the dynamic shear modulus and its maximum
 188 value. The analysis suggests that when γ_d remains below a threshold γ_{tv} , there is little permanent
 189 deformation under cyclic loading [40,43]. γ_{tv} varies within a specific range. The mean value of γ_{tv} ,
 190 denoted as $\gamma_{tv,M}$, corresponds to $G_d/G_{max} = 0.65$. Through fitting, a relationship between $\gamma_{tv,M}$ and the
 191 soil's plasticity index (I_p) emerges, as shown in Equation (5) [40]. Applying this in Equation (6) allows
 192 for the estimation of γ_r [40], which can be calculated using Equation (7). In instances where the track
 193 foundation fill has an I_p value of 0, γ_r is estimated to be 258.01×10^{-6} .



195 **Figure 5.** Curve of G_d/G_{\max} versus γ_d [43].

196
$$\gamma_{\text{tv,M}} = (209.84e^{0.036I_p} - 70.91) \times 10^{-6} \quad (5)$$

197
$$G_d/G_{\max} = 1/(1 + \gamma_d/\gamma_r) \quad (6)$$

198
$$\gamma_r = (389.70e^{0.036I_p} - 131.69) \times 10^{-6} \quad (7)$$

199 The K_{30} test mandates a loading plate settlement, s , of 1.25 mm. Soil located at a depth roughly
200 equivalent to twice the diameter of the loading plate beneath the ground surface is mainly influenced
201 by the applied loading on plate. At this depth, soil compression constitutes approximately 90% of the
202 total compression. Consequently, the average compressive strain amplitude, $(\varepsilon_d)_{K30}$, under the K_{30} test
203 condition is 1875×10^{-6} [40]. The threshold for rapid convergence of soil compression strain, denoted
204 as $[\varepsilon_{11}]$, under the working condition of track foundation during train transit, can be estimated using
205 Equation (8) [40]. Under the conditions of one-dimensional elastic compression and a constant
206 Poisson's ratio, it can be assumed that $(\gamma_d)_{K30}$ equals $(\varepsilon_d)_{K30}$, and $(\gamma_d)_t$ equals $[\varepsilon_{11}]$ [42].

207
$$[\varepsilon_{11}] = 0.28K_{30} + 107 \quad (8)$$

208 Moreover, K_{30} for upper trackbed (0 to 0.4 m), lower trackbed (0.4 to 2.7 m), and subgrade are set to
209 the minimum allowable values of 190 MPa/m, 150 MPa/m, and 130 MPa/m, respectively. The
210 allowable values are derived from *Code for Design of Railway Earth Structure* (TB10001-2016) [44].

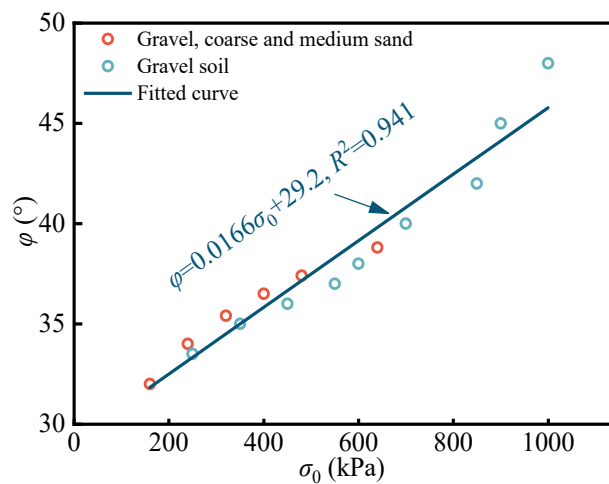
211 2.2.2. Ground parameter

212 The ground is made of coarse-grained soils. The relationship between E , E_e , and σ_0 of ground soil can
213 be indirectly approximated through Equation (9), which correlates ground bearing capacity σ_0 with K_{30}
214 [40]:

215
$$K_{30} = 0.42\sigma_0 - 6.25 \quad (9)$$

216 where K_{30} and σ_0 are expressed in MPa/m and kPa.

217 In addition, the connection between the friction angle φ of the ground soil and σ_0 can be
218 represented by a statistical relation, as illustrated in Figure 6, with data sourced from *Technical Code*
219 *for Building Foundation* (DB21/T 907-2015) [45]. The provided data align well with a linear
220 expression, as indicated in Equation (10). In this equation, φ is measured in degrees, while σ_0 is in kPa.
221 The high coefficient of determination, R^2 , which is 0.941, suggests that this linear expression
222 accurately characterizes the relationship between φ and σ_0 .



223
224 **Figure 6.** Empirical relationship between σ_0 and φ for coarse-grained ground.

225

$$\varphi = 0.0166\sigma_0 + 29.2 \quad (10)$$

226 Furthermore, the coefficient of earth pressure at rest ($K_{h,0}$) in normally consolidated soil is
227 approximately correlated with the soil friction angle φ , as described in Equation (11) [46]. Additionally,
228 the relationship between $K_{h,0}$ and Poisson's ratio μ , assuming elasticity, is demonstrated in Equation
229 (12) [47]. Subsequently, the connection between μ and φ can be approximated using Equation (13).
230 Moreover, the dilation angle, which indicates volumetric change during the shearing of coarse-grained
231 soils, is taken as 0.5φ . Therefore, the computational parameters of the ground soil in the FDM model
232 can be estimated from σ_0 , which is the basic parameter of ground considered in the design of retaining

233 wall, utilizing the aforementioned approximate relationship.

$$234 \quad K_{h,0} = 1 - \sin \varphi \quad (11)$$

$$235 \quad K_{h,0} = \frac{\mu}{1 - \mu} \quad (12)$$

$$236 \quad \mu = \frac{K_{h,0}}{1 + K_{h,0}} = \frac{1 - \sin \varphi}{2 - \sin \varphi} \quad (13)$$

237

238 **2.2.3. Interface model**

239 A collection of triangular interface elements [35] with negligible thickness are used to represent the
240 interaction between the soil and retaining wall, as well as between the concrete base and adjacent
241 structural layers in the track structure. These elements are connected to the surfaces of solid elements
242 via nodes. Each element is characterized by a normal stiffness and a shear stiffness, both set to a large
243 value of 40 GPa/m. The interface strength follows the Coulomb shear strength criterion, and the
244 maximum shear force $F_{s,max}$ required for the interface without cohesion in the model to experience
245 relative movement is calculated using Equation (14):

$$246 \quad F_{s,max} = F_n \cdot \tan \varphi_l \quad (14)$$

247 where F_n represents the normal force acting on the interface, φ_l denotes the friction angle of interface
248 materials. φ_l of wall-fill interface, as well as wall bottom-ground, are set as 0.5 and 0.6 times the
249 friction angle of the soil in contact with them.

250 **2.3. Validation**

251 This subsection demonstrates the efficacy of the FDM model via an in-situ test involving a ballasted
252 railway supported by a gravity retaining wall. Furthermore, the FDM model's capacity to portray the

253 interaction between the slab track and foundation is further confirmed through a full-scale model test.

254 2.3.1 Case 1: in-situ monitoring

255 A monitoring campaign was conducted on a railway retaining wall to validate the numerical model.

256 Figure 7 displays the characteristics of the in-situ structure [17]. The retaining wall, constructed from

257 C25 concrete, spans 20 m in length, stands 5 m high, measures 1.05 m in width, and features a gradient

258 of 1:0.25. The lower section of the wall base is filled with rammed earth to a depth of 0.5 m. The track

259 was built using C60 concrete sleepers and 60 kg/m rails. The upper roadbed material, which measures

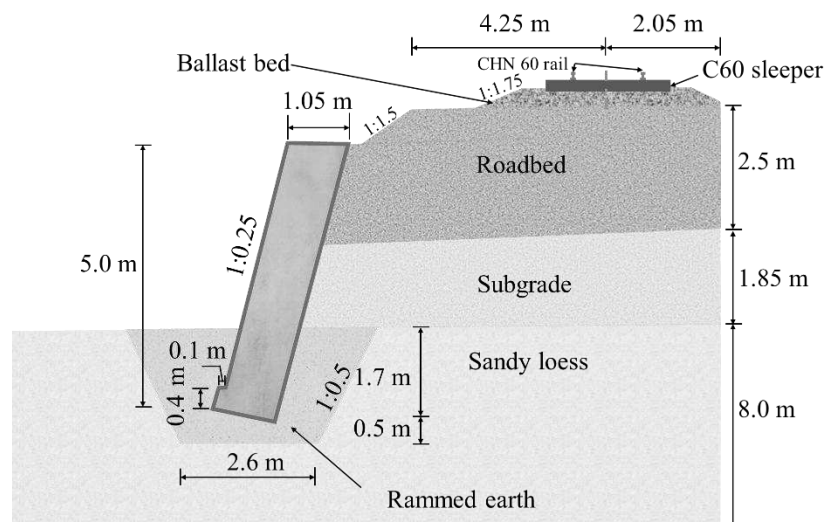
260 0.6 m in thickness, consists of graded gravel. The lower roadbed, which is 1.9 m thick, and the subgrade

261 located below it are both made of Class-A fill. The compaction degrees for the lower roadbed and the

262 subgrade are 95% and 92%, respectively. The ground is sandy loess with thickness of 8 m. The freight

263 car utilized in the test has an axle weight of 300 kN, an axle spacing of 1.86 m per bogie, and a

264 minimum axle spacing of 1.94 m between the front and rear cars.



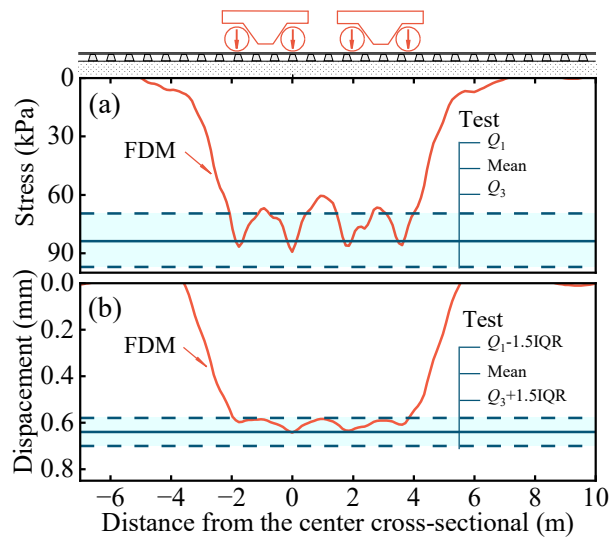
265
266 **Figure 7.** Cross-sectional view of the in-situ structure.

267 The FDM model is designed to simulate only the half of the embankment adjacent to the retaining

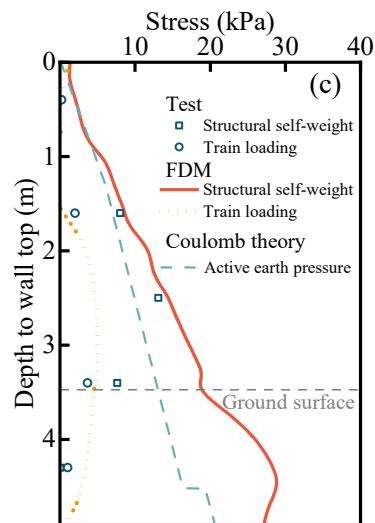
268 wall. To simulate the train loading, axle loads from two adjoining bogies of the front and rear cars are
269 utilized [48]. The amplification factor Φ_{kl} is assumed as 1.4 at speed of 100 km/h according to the code
270 [44]. Additionally, the vertical dynamic stiffness of the fasteners is 100 kN/mm [18]. The values of E
271 for the upper roadbed, the lower roadbed and the subgrade are 48.2 MPa, 37.0 MPa, and 32.0 MPa,
272 respectively. Correspondingly, the values of E_e are 241.4 MPa, 190.8 MPa, and 166.8 MPa. The ballast
273 and retaining walls are considered as elastic materials. The ballast has density of 2,130 kg/m³, μ of
274 0.30, and E_e of 300 MPa, while the retaining wall has density of 2,300 kg/m³, μ of 0.20, E_e of 28 GPa.
275 The ground material adheres to the Mohr-Coulomb failure criterion. The sandy loess soil has a density
276 of 1800 kg/m³, μ of 0.34, E of 26 MPa, E_e of 138.6 MPa, cohesion of 15kPa, φ of 29°, and a dilation
277 angle set to 0.5φ . Similarly, the rammed earth has a density of 1900 kg/m³, μ of 0.30, E of 32 MPa, E_e
278 of 167.7 MPa, cohesion of 39 kPa, and φ of 35°.

279 Figure 8 shows the stress, and displacement at the roadbed surface, as well as earth pressure behind
280 the retaining wall from FDM model and test. As shown in Figure 8a and Figure 8b, the peak values of
281 stress and displacement at the roadbed surface are in good agreement. In the figures, only the statistical
282 indicators of the measured peak values are shown, including the mean, upper quartile Q_3 , lower quartile
283 Q_1 , etc. The interquartile range (IQR) is defined as the difference between Q_3 and Q_1 . Moreover, Figure
284 8c indicates that the earth pressure on the central cross-section of the model, which is influenced by
285 the self-weight of the structure and the train loading. Comparisons between calculated and tested
286 values of earth pressures resulting from structural self-weight reveal close alignment above ground.
287 However, in regions proximate to or within the ground, the calculated values exceed the tested ones.
288 Notably, they reasonably remain higher than the active earth pressures ascertained through Coulomb

289 earth pressure theory. The discrepancy between FDM and test data is likely due to the horizontal
 290 constraint imposed by the lower soil on the backfill near the wall's base. Consequently, ensuring
 291 effective contact with the earth pressure cell mounted behind the wall becomes challenging after wall
 292 displacement. As a result, the measured values appear reduced and are less reliable. In addition, the
 293 calculated values of the earth pressure increments due to train loading are in general agreement with
 294 the test values derived from other sensors. These comparison suggests that the FDM model is suitable
 295 for analysing the deformation and force of the track foundation supported by gravity retaining wall
 296 under train loading.



297



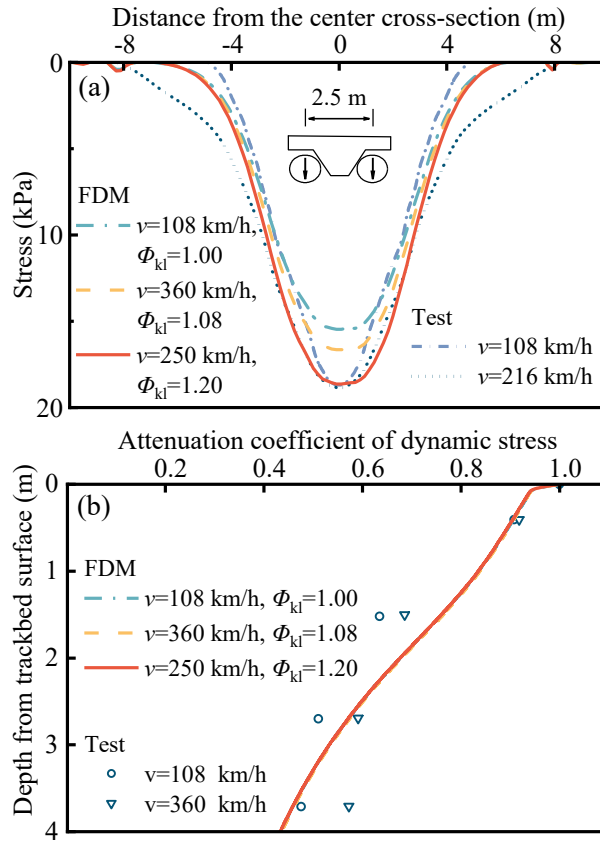
298

299 **Figure 8.** Comparison between FDM and test data: (a) stress at roadbed surface; (b) surface displacement on roadbed;
300 (c) earth pressure against the retaining wall.

301 **2.3.2 Case 2: full-scale model**

302 Bian et al. [49] conducted a dynamic test on a full-scale railway slab track model. This test involved
303 simulating train loading on the track, with an axle load of 170 kN, at different speeds. It's important to
304 note that these loads did not consider the impact of track irregularities, resulting in a relatively small
305 amplification factor, Φ_{kl} [24,49]. When simulating a train speed of 108 km/h using the FDM, the bogie
306 loads matched a Φ_{kl} of 1.00. In contrast, a speed of 360 km/h resulted in a Φ_{kl} of 1.08 [49]. Figure 9
307 illustrates the stress distribution within the foundation induced by single bogie loading, as determined
308 by both the test and FDM. In addition to verifying the FDM model through the loading conditions in
309 the tests, Figure 9 also shows the stress distribution when Φ_{kl} is taken as 1.20 for the study of retaining
310 wall supported track foundation. At the center of the track structure, the stress on the surface of the
311 trackbed due to dual-axle loading diminishes symmetrically from the center towards both sides along
312 the longitudinal direction, as depicted in Figure 9a. In addition, the stress within the foundation soil
313 gradually attenuates with increasing depth, as presented in Figure 9b. The FDM data indicates that the
314 load magnitude does not significantly affect the attenuation coefficient's variation with depth under
315 single bogie loading. Overall, the close agreement between the test and FDM data further confirms the
316 effectiveness of the FDM model in capturing the characteristics of a slab track foundation under train
317 loading.

318



319

320 **Figure 9.** Stress within the ballastless railway foundation: (a) distribution on the trackbed surface; (b) attenuation
 321 coefficients along depth.

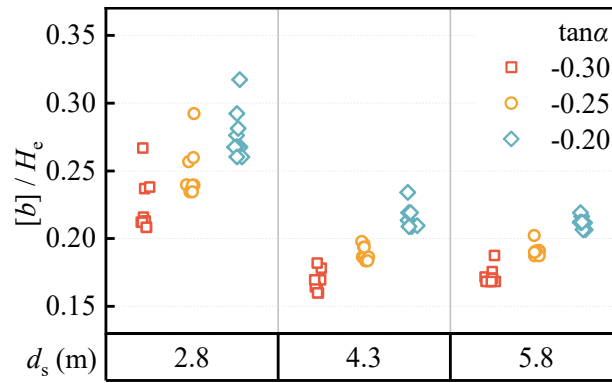
322 3. Assessment method

323 Five factors that are important for evaluating the influence of a landward-leaning retaining wall on
 324 train-induced trackbed surface displacement include: σ_0 , H_e , $\tan\alpha$, d_s , and b/H_e . Table 2 displays the
 325 values of the variables in investigation, consisting of a total of 351 permutations with the wall face and
 326 the wall back remaining parallel. Structural stability may be compromised if the value of b is too small.
 327 The minimum width of the wall, which precisely satisfies the stability requirements [19] when other
 328 parameters are determined, is denoted by $[b]$. Among all combinations of σ_0 , H_e , $\tan\alpha$, and d_s , the ratio
 329 of $[b]$ to H_e is significantly impacted by d_s and $\tan\alpha$. The correlation between $[b]/H_e$ and d_s and $\tan\alpha$ is
 330 demonstrated in Figure 10, showing that the value of $[b]/H_e$ increases as the wall approaches the track
 331 structure (d_s decreases) or as the inclination of the wall becomes steeper ($\tan\alpha$ increases). As a result,

332 the minimum value of b/H_e in Table 2 differs depending on the values of d_s and $\tan\alpha$. It is not cost-
 333 effective to use gravity retaining walls with excessively large values of b to support foundations, and
 334 a maximum value of 0.35 times H_e is chosen.

335 **Table 2.** Discrete alternatives of the retaining wall parameters.

Variables	Min. value	Max. value	Increment
σ_0 (kPa)	300	900	300
H_e (m)	3.0	7.0	2.0
$\tan\alpha$	-0.30	-0.20	0.05
d_s (m)	2.8	5.8	1.5
b/H_e	0.25, if $d_s = 2.8$ m and $\tan\alpha = -0.20$; 0.20, if $d_s = 2.8$ m and $\tan\alpha \neq -0.20$; 0.20, if $d_s \neq 2.8$ m and $\tan\alpha = -0.20$; 0.15, if $d_s \neq 2.8$ m and $\tan\alpha \neq -0.20$	0.35	0.05



336
 337 **Figure 10.** Effects of d_s and $\tan\alpha$ on $[b]/H_e$.

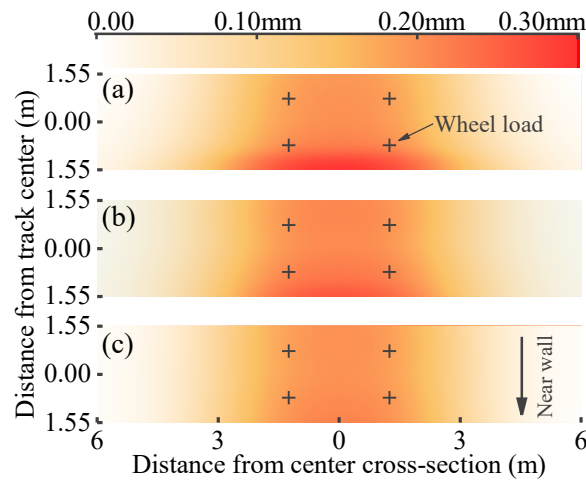
338 3.1. Data characteristics

339 Three representative cases, namely, Cases A, B, and C, determined from the parameters in Table 3,
 340 were selected to illustrate the characteristics of the trackbed surface displacement ω . Figure 11 displays
 341 the planar distribution pattern of ω . For the concentration of ω primarily exists within the track's
 342 transverse direction, its distribution outside the track base remains absent from Figure 11. Observations
 343 suggest a gradual decline of ω in the longitudinal direction from the centre of bogie loading towards
 344 the peripheries. Notably, the contributing factors in the performance assessment of retaining walls have
 345 potentially significant impact on the magnitude of ω at the track structure edge proximal to the wall.

346 To explain the magnitude law of ω in Figure 11, Figure 12 presents the strain increment contours of
 347 soils observed at the central cross-section of the bogie corresponding to the three cases.

348 **Table 3.** Retaining wall design parameters for cases exhibiting the characteristics of the ω distribution.

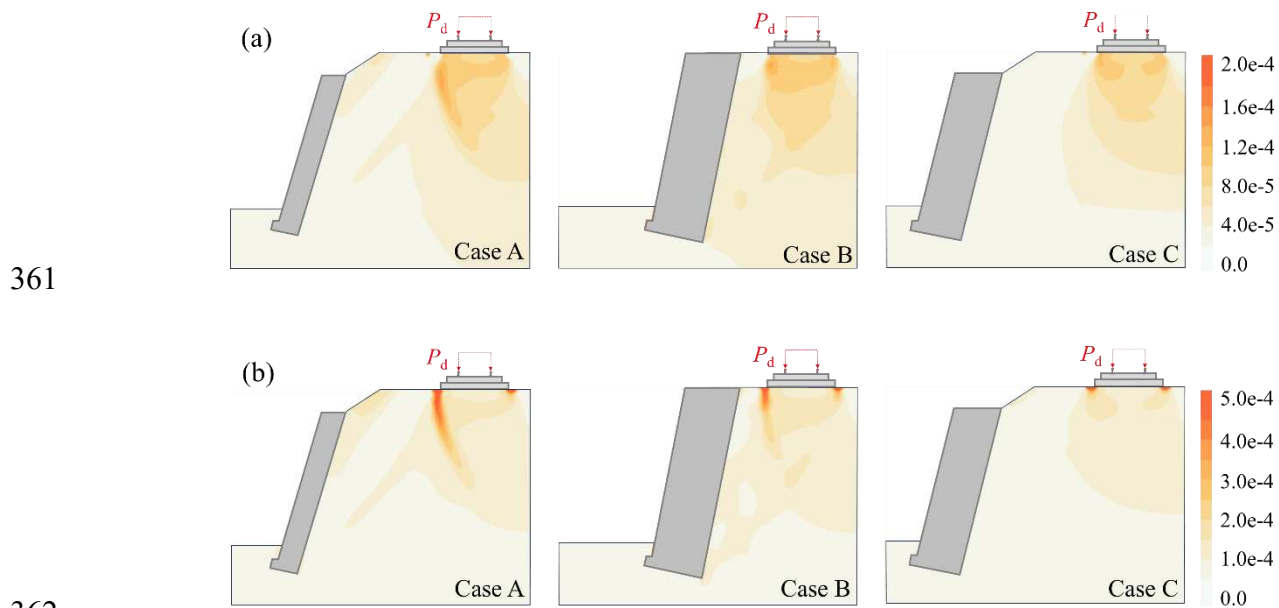
Case	σ_0 (kPa)	H_e (m)	$\tan\alpha$	d_s (m)	b/H_e
A	300	7	-0.3	5.8	0.15
B	300	7	-0.2	2.8	0.35
C	900	7	-0.2	5.8	0.35



349
 350 **Figure 11.** Planar distribution patterns of ω : (a) Case A; (b) Case B; (c) Case C.

351 The trackbed soil supported by the retaining wall in Case A, as shown in Figure 12a, exhibits a larger
 352 vertical strain increment beneath the track structure than Cases B and C. In particular, the distribution
 353 of vertical strain increment in the soil beneath the track edge near the wall shows a curved profile and
 354 is substantially greater than in the other cases. This profile results in vertical displacements in both the
 355 track structure and trackbed surface within the corresponding region. Moreover, Case A shows the
 356 formation of curved strips with significantly higher values of maximum shear strain increment in the
 357 soil beyond the track edge adjacent to the wall under train loading, as demonstrated in Figure 12b. The
 358 soil beneath the track undergoes sliding displacement along the curved strips of higher maximum shear
 359 strain while undergoing compressed deformation. Consequently, a greater ω appears at the track

360 structure edge near the wall in Figure 11a compared to Figure 11b and c.

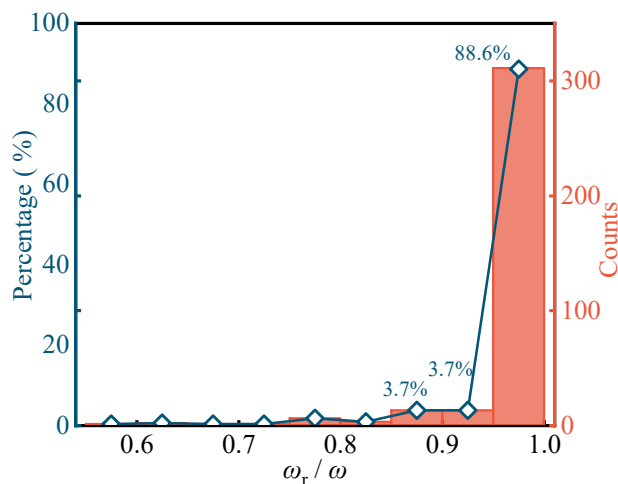


362
363 **Figure 12.** Contours: (a) vertical strain increment; (b) maximum shear strain increment.

364 Comparative analysis of ω at the edges of the track in the cross-section of the bogie centre reveals a
365 trend: values of ω adjacent to the wall are typically higher than those further away. Specifically, ω
366 measurements close to the wall vary between 0.206 mm and 0.499 mm. In contrast, values on the
367 opposite side range from 0.188 mm to 0.230 mm. The former is more greatly influenced by factors
368 such as σ_0 , H_e , $\tan\alpha$, d_s , and b/H_e . Thus, the value of ω at the track edge near the wall on the central
369 cross-section of the bogie can be used as an indicator for assessing the performance of the retaining
370 wall-supported track foundation.

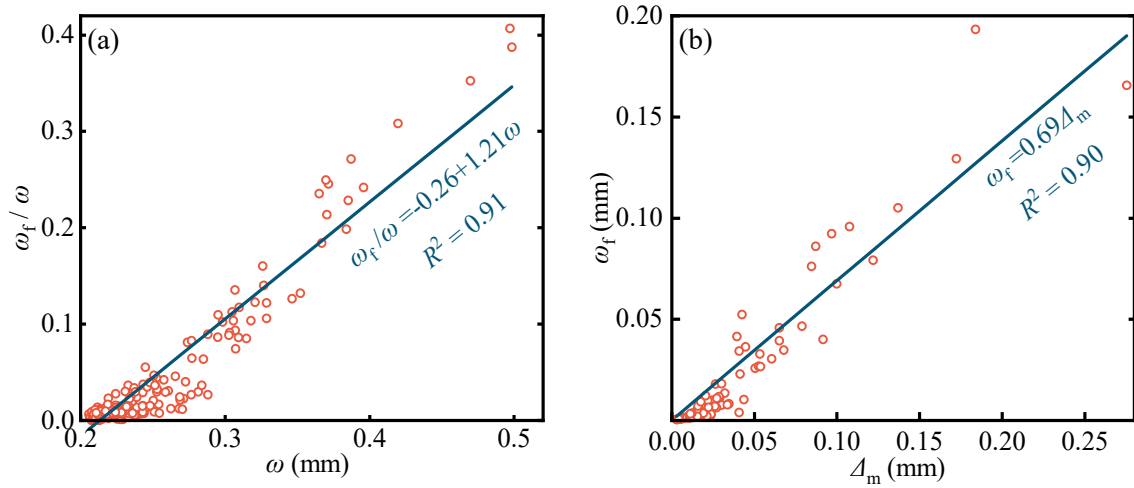
371 Figure 13 presents the statistics for the ratio of ω_r to ω at the track edge near the wall in the central
372 cross-section of the bogie. Only 4.0% of the samples have ω_r/ω values below 0.85, with the minimum
373 value being greater than 0.55. In contrast, approximately 88.6% of the total samples have ω_r/ω values
374 above 0.95, highlighting the influential role of ω_r on ω . This suggests that reinforcing the existing

375 retaining wall might not significantly diminish train-induced displacement on the trackbed surface.



376
377 **Figure 13.** The distribution of the ratio of ω_r to ω .

378 Figure 14 depicts the correlation between ω_f and ω , as well as between ω_f and Δ_m . Here, Δ_m denotes
379 the horizontal displacement of the wall at its vertical mid-point induced by train loading. As shown in
380 Figure 14a, there is a linear correlation between ω_f/ω and ω , especially notable at higher ω values.
381 Notably, the values of ω are larger when the retaining wall restrained the embankment soil weakly.
382 Under such circumstances, ω_f , which arises from wall displacement due to train loading, constitutes a
383 larger fraction of ω . Furthermore, Figure 14b indicates a linear positive correlation between ω_f and Δ_m ,
384 with the former being approximately 0.69 times the latter. The fitted linear expressions shown in Figure
385 14 exhibit a coefficient of determination (R^2) equal to or exceeding 0.9, signifying a robust linear
386 correlation between these variables.



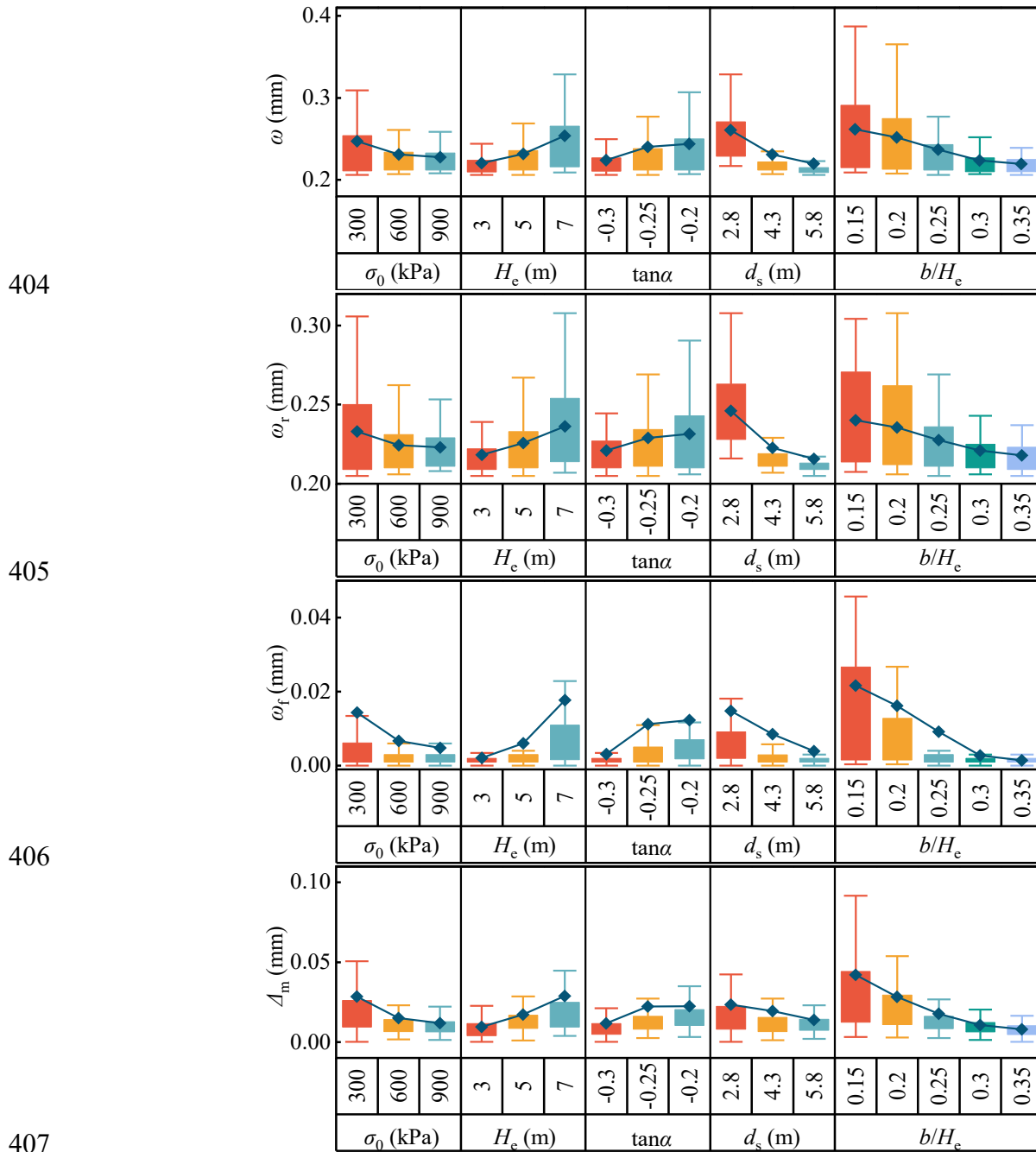
387

388 **Figure 14.** Relationship: (a) between ω_f and ω ; (b) between ω_f and Δ_m .

389 Boxplots were used to analyse the distributions of ω , ω_r , ω_f and Δ_m in relation to each variable, as
 390 shown in Figure 15. The interquartile range (IQR), representing the middle 50% of the data, is
 391 indicated by the rectangular box within the boxplots. The whisker arms extend to 1.5 times the IQR,
 392 depicting the distribution of the remaining data points. Additionally, a line connects the average values
 393 of the parameter datasets, providing a comprehensive view of the pattern.

394 It is evident that adjusting the values of σ_0 , H_e , $\tan\alpha$, d_s or b/H_e results in a consistent trend in the
 395 average values of the indicators ω , ω_r , ω_f and Δ_m , as shown in Figure 15. An increase in σ_0 improves
 396 the ability of the ground to restrain the base of the retaining wall. Reducing H_e or $\tan\alpha$, or increasing
 397 d_s can mitigate the interference of wall in the foundation soil and the impact of train loading on the
 398 wall. Additionally, increasing b/H_e , i.e. thickening the wall, enhances its ability to withstand earth
 399 pressure through self-weight. All of these trends lead to a decrease in ω , ω_r , ω_f , and Δ_m , thereby aiding
 400 in the management of wall displacement and soil deformation behind the wall. Moreover, the
 401 concentration of indicators is greater under optimal conditions, indicating adjusting factors to ensure
 402 sufficient support capacity of the retaining wall can stabilize the deformation of track foundation within

403 a narrower range.



408 **Figure 15.** Distribution of ω , ω_r , ω_f and Δ_m with respect to each variable value.

409 **3.2. Evaluation model**

410 The index of trackbed surface displacement, denoted as R_ω , is defined as the ratio of the maximum

411 allowable value $[\omega]$ of trackbed surface displacement caused by train loading to the calculated ω at the

412 track edge near the wall on the centre cross-section of the bogie. This index quantifies the restraining
413 ability of the retaining wall in limiting the deformation of track foundation. A higher R_ω value signifies
414 stronger restraint exerted by the retaining wall over the fill material. R_ω value of 1.0 or more suggests
415 that the actual displacement does not exceed the allowable limit $[\omega]$. According to the technical
416 specification [44], the recommended value of $[\omega]$ is 0.22 mm, slightly exceeding the maximum ω of
417 the standard embankment supported by the slope soil (as determined via the FDM). To evaluate the
418 support capacity of the retaining wall, a MARS prediction model for R_ω was developed using the py-
419 earth library in Python 3.10, based on data from 351 track foundations supported by landward-leaning
420 walls.

421 **3.2.1. Methodology**

422 The MARS algorithm, introduced by Friedman [36], is a non-parametric and nonlinear regression
423 technique capable of modelling relationships between input and output variables [50,51]. It operates
424 by employing a sequence of linear segments with distinct slope. The end points of these segments are
425 denoted as knots [52]. The construction of the MARS model is performed in two phases. The adaptive
426 regression algorithm selects potential knots during the forward phase, and basis functions (BFs) are
427 gradually searched for fitting until the maximum number of terms is reached. This process produces
428 an overfitted model, and during the backward phase, the generalized cross-validation (GCV) criterion
429 is used to eliminate BFs with minimal influence. This reduces the degree of overfitting and prevents
430 the MARS model from containing an excessive number of terms. The MARS model can be explicitly
431 expressed using Equation (15):

432
$$f(X) = \beta_0 + \sum_i^I \beta_i \lambda_i(X) \quad (15)$$

433 where $f(X)$ is the output variable value predicted by the model. β_0 represents a constant term, whereas
 434 β_i signifies the coefficient of the i^{th} basis function. $\lambda_i(X)$ denotes the i^{th} basis function. I signifies the
 435 predefined maximum number of BFs. Notably, the spline function can be configured as a piecewise
 436 linear function, expressed by Equation (16):

437
$$\max(0, x - \zeta) = \begin{cases} x - \zeta, & \text{if } x \geq \zeta \\ 0, & \text{if } x < \zeta \end{cases} \quad (16)$$

438 where ζ represents a certain value of x .

439 The value of GCV can be determined using Equation (17):

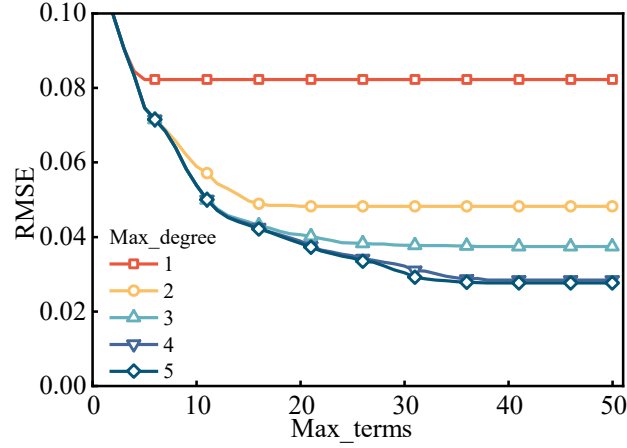
440
$$\text{GCV} = \frac{\frac{1}{L} \sum_{l=1}^L [y_l - f(X_l)]^2}{\left[1 - \frac{I + g(I - 1) / 2}{L}\right]^2} \quad (17)$$

441 where L represents the number of observations, y_l denotes the actual value of the l^{th} observation,
 442 $f(X_l)$ is the predicted values of the MARS model, and g represents the penalizing parameter.

443 3.2.2. MARS-based model

444 To train the MARS model, the parameters “max_terms” and “max_degree” used in the forward phase
 445 must be determined. “Max_terms” specifies the maximum number of BFs allowed, while “max_degree”
 446 indicates the highest degree of the BFs. An exhaustive search across all combinations is conducted,
 447 with max_terms ranging from 1 to 50 and max_degree from 1 to 5, both in increments of 1. The optimal
 448 parameter values with lowest root mean square error (RMSE) are determined using five-fold cross-
 449 validation. As shown in Figure 16, RMSE stabilizes and the performance of the MARS model ceases
 450 to improve when max_terms ≥ 36 and max_degree ≥ 4 . Consequently, the optimal values for the two

451 parameters are determined to be 36 and 4, respectively.



452
453 **Figure 16.** Effects of max_terms and max_degree on RMSE.

454 The MARS model's training involved using 80% of the sample data for the training set, with the
455 remaining 20% as the test set. The resulting predictive equation for R_ω , denoted as Equation (18),
456 contains 30 BFs, whose definitions can be found in Table 4. The R_ω values for the training set ranged
457 from 0.442 to 1.069, with an average of 0.959 and a standard deviation of 0.124. The predicted R_ω
458 values varied between 0.438 to 1.081, with an average of 0.959 and a standard deviation of 0.120,
459 indicating a close similarity between the predicted values and the FDM values.

$$\begin{aligned}
 R_\omega = & -1.40 + 1.35 \times B_1(X) + 2.88 \times B_2(X) - 2.05 \times B_3(X) - 6.96 \times B_4(X) + 10.41 \times B_5(X) \\
 & + 25.23 \times B_6(X) - 19.36 \times B_7(X) - 7.18 \times 10^{-2} \times B_8(X) - 2.81 \times B_9(X) + 1.10 \times 10^{-4} \times B_{10}(X) \\
 & + 1.43 \times 10^{-3} \times B_{11}(X) + 0.37 \times B_{12}(X) + 1.44 \times 10^{-3} \times B_{13}(X) - 0.56 \times B_{14}(X) + 2.31 \times B_{15}(X) \\
 & + 13.09 \times B_{16}(X) + 0.27 \times B_{17}(X) - 20.25 \times B_{18}(X) - 7.32 \times B_{19}(X) - 6.13 \times 10^{-7} \times B_{20}(X) \\
 & - 3.80 \times 10^{-4} \times B_{21}(X) + 18.88 \times B_{22}(X) + 0.05 \times B_{23}(X) - 2.66 \times 10^{-3} \times B_{24}(X) - 0.13 \times B_{25}(X) \\
 & + 1.00 \times 10^{-7} \times B_{26}(X) + 3.92 \times 10^{-5} \times B_{27}(X) - 5.00 \times 10^{-5} \times B_{28}(X) - 2.60 \times 10^{-2} \times B_{29}(X) \\
 & + 9.45 \times B_{30}(X)
 \end{aligned} \tag{18}$$

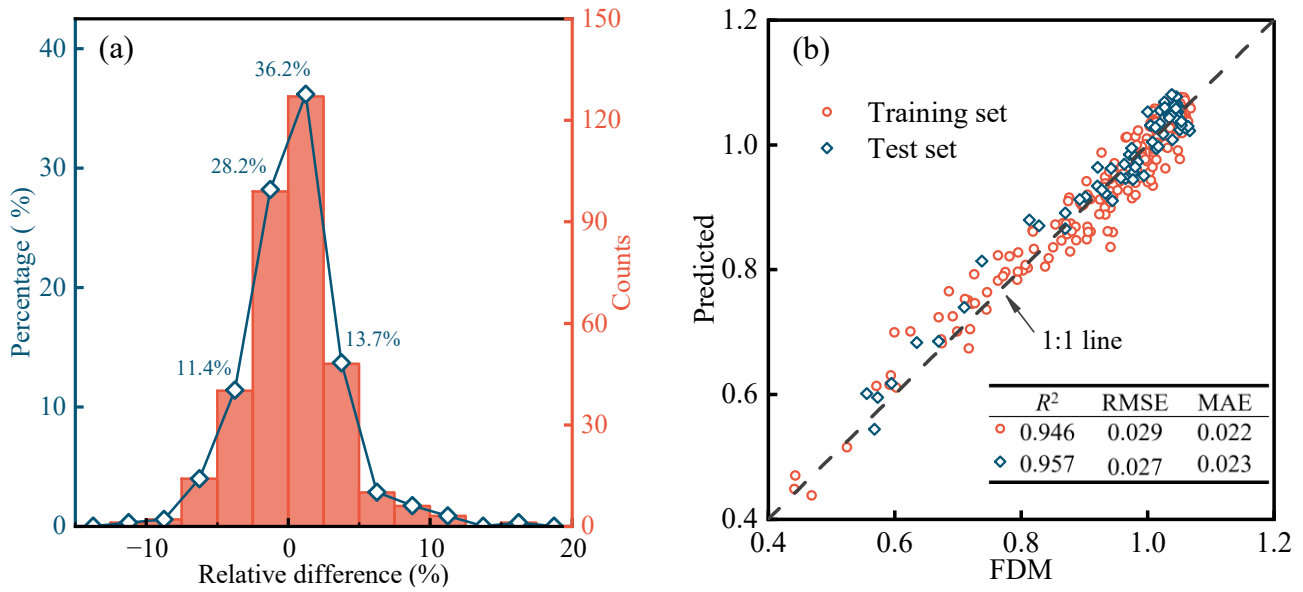
461 **Table 4.** Basis functions of the developed MARS model.

BFs	Formula	BFs	Formula	BFs	Formula
$B_1(X)$	X_4	$B_{11}(X)$	$X_0X_3X_2X_1$	$B_{21}(X)$	X_0X_4
$B_2(X)$	X_3	$B_{12}(X)$	$X_2X_4X_4$	$B_{22}(X)$	$X_2X_3X_2X_1$
$B_3(X)$	X_1	$B_{13}(X)$	X_0	$B_{23}(X)$	X_1X_4
$B_4(X)$	X_2X_1	$B_{14}(X)$	$X_3X_2X_4X_4$	$B_{24}(X)$	$X_1X_1X_4$

$B_5(X)$	X_1X_3	$B_{15}(X)$	$X_3X_3X_4$	$B_{25}(X)$	$X_1X_3X_2X_1$
$B_6(X)$	$X_3X_2X_1$	$B_{16}(X)$	$X_3X_3X_1X_3$	$B_{26}(X)$	$X_4X_0X_0$
$B_7(X)$	$X_3X_1X_3$	$B_{17}(X)$	$X_4X_3X_2X_1$	$B_{27}(X)$	$X_3X_0X_4X_4$
$B_8(X)$	X_4X_4	$B_{18}(X)$	$X_3X_3X_2X_1$	$B_{28}(X)$	$X_0X_2X_4X_4$
$B_9(X)$	X_3X_4	$B_{19}(X)$	$X_2X_2X_1$	$B_{29}(X)$	$X_4X_2X_4X_4$
$B_{10}(X)$	X_0X_1	$B_{20}(X)$	X_0X_0	$B_{30}(X)$	$X_2X_2X_3$

462 Note: X_0 represents the bearing capacity σ_0 of ground; X_1 denotes the height H_e of the embankment; X_2 corresponds
463 to the tangent value $\tan\alpha$ of the inclination angle of the wall back, with a negative value for landward-leaning wall;
464 X_3 indicates the ratio of the wall width to the height of the embankment, i.e., b/H_e ; X_4 refers to the distance d_s between
465 the centerline of the track near the wall and the vertex of the wall back.

466 Figure 17 compares the values of R_ω from FDM with the MARS predicted values. The distribution of
467 relative difference is shown in Figure 17a, where it can be seen 89.5% of the samples have a relative
468 difference within $\pm 5.0\%$, with only a few samples exceeding $\pm 10.0\%$. Additionally, Figure 17b
469 illustrates the correlation between predicted and calculated values of R_ω , with a scatter plot closely
470 aligned to the 1:1 line. This suggests a strong similarity between the predicted and calculated values.
471 In addition, the training set has a coefficient of determination R^2 of 0.946, a RMSE of 0.029, and a
472 mean absolute error (MAE) of 0.022, indicating the model has captured the relationship between the
473 input variables and R_ω from the training set. For the test set, the R^2 is 0.957, with RMSE and MAE
474 values of 0.027 and 0.023, respectively, demonstrating the model's robust generalizability. Hence, it
475 was concluded that the MARS model is capable of expressing the relationship between σ_0 , H_e , $\tan\alpha$,
476 b/H_e , d_s and R_ω .

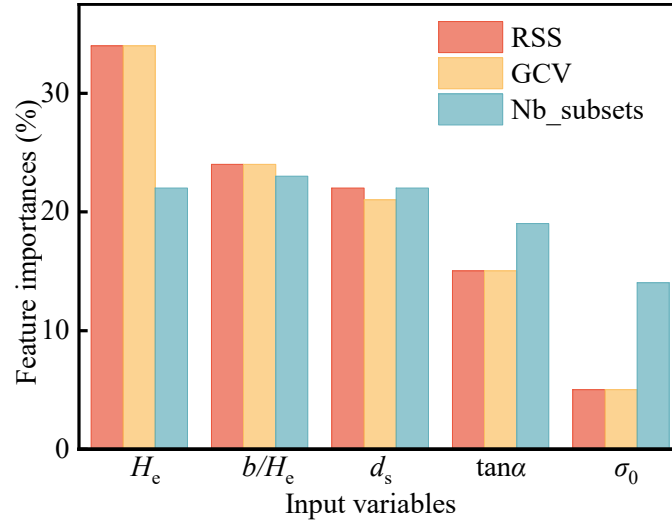


477

478 **Figure 17.** Comparison between predicted and FDM value of R_ω : (a) the relative difference; (b) the values.

479 **3.3. Parametric study**

480 Figure 18 illustrates the feature importance of input variables considered in MARS model, as estimated
 481 by residual sum-of-squares (RSS), GCV, and nb_subsets criterion. The analysis indicates that R_ω is
 482 influenced primarily by the height (H_e) of the embankment supported by the retaining wall, the ratio
 483 of wall width to embankment height (b/H_e), and the distance (d_s) between the wall and the track.
 484 Conversely, the inclination of the wall ($\tan\alpha$) and the ground bearing capacity (σ_0) have a lesser impact
 485 on R_ω .



486

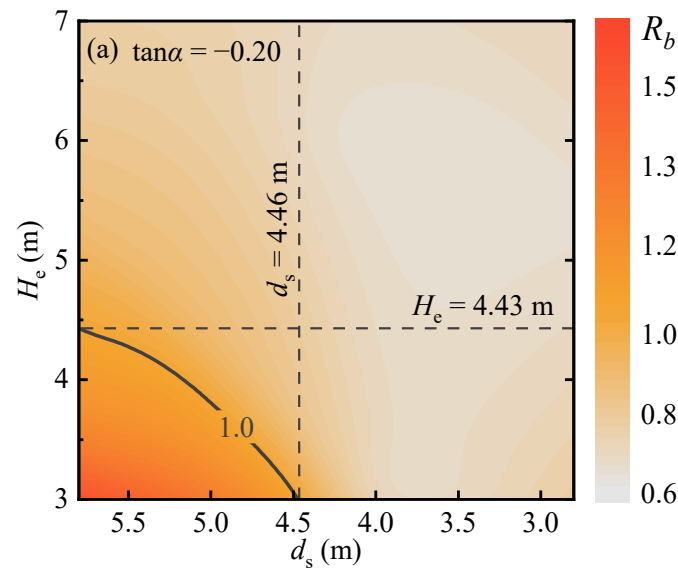
487 **Figure 18.** Feature importance of the input variables.

488 Additionally, correlation analysis based on correlation coefficient [53] was conducted to quantify the
 489 relationships between these factors and R_ω . The correlation coefficients for H_e , b/H_e , d_s , $\tan\alpha$, and σ_0
 490 with R_ω are -0.327 , 0.343 , 0.449 , -0.194 , and 0.157 , respectively. This analysis further indicates that
 491 R_ω has a strong correlation with H_e , b/H_e , and d_s , but only a weak correlation with $\tan\alpha$ and σ_0 . Notably,
 492 R_ω is negatively correlated with H_e and $\tan\alpha$ and positively correlated with the other factors.

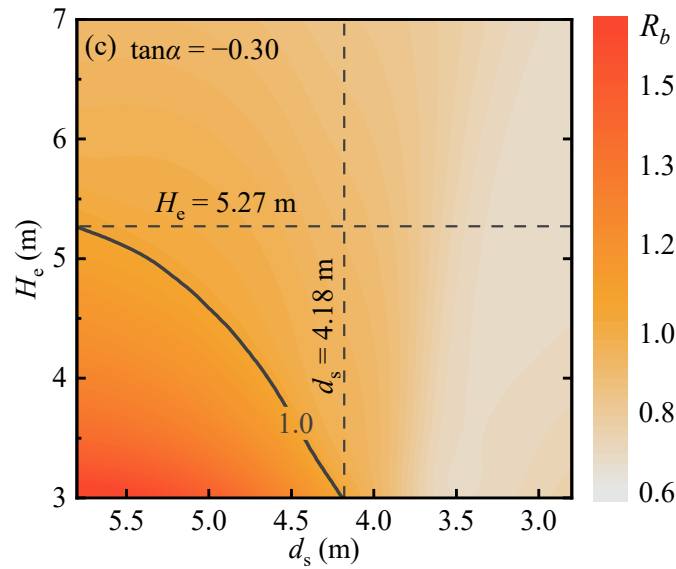
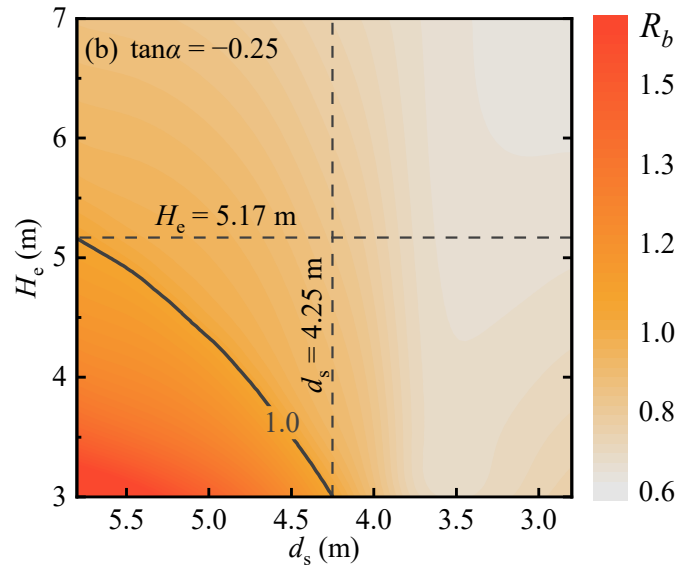
493 After determining the values of d_s , $\tan\alpha$, σ_0 , and H_e , the initial minimum value of b is set as $b_{\min} =$
 494 0.2 m, and the initial maximum value of b is set as $b_{\max} = 0.45H_e$. Next, the MARS model was used to
 495 estimate R_ω by setting $b = (b_{\max} + b_{\min})/2$. Then, if $R_\omega \geq 1.0$, update b_{\max} to b ; or alternatively, if $R_\omega <$
 496 1.0 , update b_{\min} to b . Repeat this process until the convergence of $b_{\max} - b_{\min} \leq 0.001$ m, at which point
 497 the value of $[b_\omega] = (b_{\max} + b_{\min})/2$ corresponds to $R_\omega = 1.0$. Figure 19 depicts an analysis of the influence
 498 of d_s , H_e , and $\tan\alpha$ on R_b , which represents the ratio of $[b]$ to $[b_\omega]$ considering $\sigma_0 = 300$ kPa. When $\tan\alpha$
 499 $= -0.20$, the circular contour line with $R_b = 1.0$ intersects the abscissa and ordinate at $d_s = 4.46$ m and
 500 $H_e = 4.43$ m respectively, as shown in Figure 19a. Within the circular arc, where d_s is greater and H_e is

501 lower, $R_b \geq 1.0$ signifies that the wall with adequate stability is effective in restricting ω to within the
 502 allowable limit. Conversely, in the exterior region of the circular arc, where d_s decreases and H_e
 503 increases, $R_b < 1.0$ indicates the wall, despite its qualified stability, lacks the necessary support capacity
 504 to effectively control ω .

505 Figure 19b and c demonstrate the influence of d_s and H_e on R_b when $\tan\alpha$ decreases further to
 506 -0.25 and -0.30 . The decrease of $\tan\alpha$ represents reduced wall inclination. The horizontal intercepts
 507 of the arc-shaped contours for $R_b = 1.0$ decrease to $d_s = 4.25$ m and 4.18 m, while the vertical intercepts
 508 increase to $H_e = 5.17$ m and 5.27 m. As a result, the inner area of the arc is enlarged and R_b is increased.
 509 Therefore, it can be inferred that the retaining wall with $\tan\alpha = -0.30$ is the most effective in controlling
 510 ω .



511



512

513

514 **Figure 19.** The impact of H_c and d_s on R_b : (a) $\tan\alpha = -0.20$; (b) $\tan\alpha = -0.25$; (c) $\tan\alpha = -0.30$.

515 4. Conclusions

516 This study used the finite difference model to examine gravity retaining walls in the context of
 517 controlling trackbed surface displacement (ω) caused by train loading. A regression model, employing
 518 the MARS algorithm, was developed to assess the supporting capacity of walls. The following
 519 conclusions were drawn:

520 (1) ω is greatly influenced by gravity retaining wall, particularly in the vicinity of the track edge

521 adjacent to the wall. Train loading tends to induce vertical compressive strain and shear strain within
522 the inner and outer soils adjacent to the track edge that is near the wall, respectively. The collective
523 effect of these strains results in larger ω . This effect is more pronounced in foundations with inadequate
524 retaining wall support.

525 (2) Despite restraining the wall from moving, ω at the track edge adjacent to the wall is significant,
526 accounting for at least 0.55 times of the total displacement. This proportion reaches its minimum only
527 when the retaining wall's supporting capacity is highly insufficient. Moreover, the increment of the
528 total value of ω , compared to that with a restrained wall, is approximately 0.69 times the train-induced
529 horizontal displacement of the wall at half its height.

530 (3) The effectiveness of a retaining wall in limiting foundation deformation due to train loading
531 primarily depends on the embankment height (H_e) it supports, the ratio of the wall's width to the
532 embankment's height (b/H_e), and the distance (d_s) between the wall and the track. In contrast, the wall's
533 inclination ($\tan\alpha$) and the ground's bearing capacity (σ_0) exert a less influence on this restraining ability.
534 There is a negative correlation between the ability and both H_e and $\tan\alpha$, while a positive correlation
535 exists with the other factors.

536 (4) To prevent ω from exceeding its limit value, further reinforcing the retaining wall is necessary,
537 in addition to a qualified stability, especially when H_e is larger or d_s is smaller. The study compared
538 the wall width needed for maximum allowable ω (as per the MARS model) with the minimum width
539 required for stability. The results show that the landward-leaning wall supporting foundations should
540 significantly increase its support capacity to manage ω effectively while ensuring stability when $H_e \geq$
541 4.43 m or $d_s \leq 4.46$ m at $\sigma_0 = 300$ kPa. And walls constructed with a gentler slope exhibit more

542 favorable limitations on ω while satisfying the stability assessment.

543 It should be noted that future studies on deformation of track foundation supported by retaining
544 walls under train loading will incorporate additional parameters. These include the axle weight, axle
545 base, and the distance between bogies of adjacent vehicles, all of which influence the effect of train
546 loading. Furthermore, constraints at the longitudinal ends of the retaining walls will also be considered
547 as significant factor.

548 **Acknowledgments**

549 This work was supported by the National Natural Science Foundation of China under grant number
550 52078435, the Natural Science Foundation of Sichuan Province under grant number 2023NSFSC0391,
551 and the 111 Project under grant number B21011.

552 **References**

- 553 [1] Jamsawang P, Voottipruex P, Jongpradist P, et al. Field and three-dimensional finite element
554 investigations of the failure cause and rehabilitation of a composite soil-cement retaining wall.
555 *Engineering Failure Analysis*. 2021;127:105532.
- 556 [2] Nakamura S. Reexamination of mononobe-okabe theory of gravity retaining walls using
557 centrifuge model tests. *Soils and Foundations*. 2006;46:135–146.
- 558 [3] Varga R, Žlender B, Jelušič P. Multiparametric analysis of a gravity retaining wall. *Applied*
559 *Sciences*. 2021;11:6233.
- 560 [4] Zhang S, Su Z, Zhong Y. Study on optimum cross-section of gravity retaining wall based on
561 ANSYS. *Advanced Materials Research*. 2011;243–249:2618–2622.
- 562 [5] Li X, Zhao S, He S, et al. Seismic stability analysis of gravity retaining wall supporting $c-\phi$ soil
563 with cracks. *Soils and Foundations*. 2019;59:1103–1111.
- 564 [6] He F, Guo G, Zhou Z, et al. Numerical simulation on soil pressure distribution characteristics of
565 gravity retaining wall. *Applied Mechanics and Materials*. 2013; 477–478: 562–566.
- 566 [7] Feng G, Luo Q, Wang T, et al. Frequency spectra analysis of vertical stress in ballasted track
567 foundations: influence of train configuration and subgrade depth. *Transportation Geotechnics*.
568 2024;44:101167.

- 569 [8] Chen H, Chen F, Lin Y. Slip-line solution to earth pressure of narrow backfill against retaining
570 walls on yielding foundations. *International Journal of Geomechanics*. 2022;22:04022051.
- 571 [9] Ma S, Jia H, Liu X. Effect of the wall-back inclination angle on the inertial loading distribution
572 along gravity-retaining walls: an experimental study on the shaking table test. *Advances in Civil
573 Engineering*. 2022; 2022 :8632920.
- 574 [10] Cao W, Liu T, Xu Z. Calculation of passive earth pressure using the simplified principal stress
575 trajectory method on rigid retaining walls. *Computers and Geotechnics*. 2019;109:108–116.
- 576 [11] Cao W, Zhang H, Liu T, et al. Analytical solution for the active earth pressure of cohesionless
577 soil behind an inclined retaining wall based on the curved thin-layer element method. *Computers
578 and Geotechnics*. 2020;128:103851.
- 579 [12] Fan X, Xu C, Liang L, et al. Analytical solution for displacement-dependent passive earth
580 pressure on rigid walls with various wall movements in cohesionless soil. *Computers and
581 Geotechnics*. 2021;140:104470.
- 582 [13] Fox PJ. Analytical solutions for active lateral earth force. *Journal of Geotechnical And
583 Geoenvironmental Engineering*. 2022;148:06022005.
- 584 [14] Qi Y, Xiao S. Inclined slice method for passive earth pressure on rigid walls considering
585 interslice shear forces. *Int J Geomech*. 2024;24:04023284.
- 586 [15] Zhou XP, Xie YX, Huang XC, et al. Antislip stability analysis of gravity retaining wall by
587 probabilistic approach. *International Journal of Geomechanics*. 2019;19:04019045.
- 588 [16] Pain A, Choudhury D, Bhattacharyya SK. Seismic rotational stability of gravity retaining walls
589 by modified pseudo-dynamic method. *Soil Dynamics and Earthquake Engineering*.
590 2017;94:244–253.
- 591 [17] Feng G, Zhang L, Luo Q, et al. Monitoring the dynamic response of track formation with
592 retaining wall to heavy-haul train passage. *International Journal of Rail Transportation*. 2022;1–
593 19.
- 594 [18] Feng G, Luo Q, Lyu P, et al. An analysis of dynamics of retaining wall supported embankments:
595 towards more sustainable railway designs. *Sustainability*. 2023;15:7984.
- 596 [19] Lyu P, Luo Q, Wang T, et al. Railway gravity retaining wall design using the flower pollination
597 algorithm. *Transportation Geotechnics*. 2023;42:101065.
- 598 [20] Xie T, Luo Q. Macroscopic embodiment of stress–strain behavior of backfill soil on the
599 displacement-dependent earth pressure curve. *Int J Geomech*. 2018;18:04018178.
- 600 [21] Wang L, Xiao S. Calculation method for displacement-dependent earth pressure on a rigid wall
601 rotating around its base. *Int J Geomech*. 2021;21:04021132.

- 602 [22] Li H, Zhang Z. Centrifugal model tests of balance weight retaining walls under translation
603 movement. ICLEM 2014: System Planning, Supply Chain Management, and Safety. Shanghai:
604 ASCE; 2014. p. 545–549.
- 605 [23] Guo Y, Zhai W, Sun Y. A mechanical model of vehicle-slab track coupled system with
606 differential subgrade settlement. *Structural Engineering and Mechanics*. 2018;66:15–25.
- 607 [24] Xie H, Luo Q, Wang T, et al. Stochastic analysis of dynamic stress amplification factors for slab
608 track foundations. *International Journal of Rail Transportation*. 2023;1–23.
- 609 [25] Ye Q, Luo Q, Feng G, et al. Stress distribution in roadbeds of slab tracks with longitudinal
610 discontinuities. *Railw Eng Science*. 2023;31:61–74.
- 611 [26] Zhu S, Luo J, Wang M, et al. Mechanical characteristic variation of ballastless track in high-
612 speed railway: effect of train–track interaction and environment loads. *Railw Eng Science*.
613 2020;28:408–423.
- 614 [27] Fu L, Zheng Y, Qiu Y, et al. Inconsistent effect of dynamic load waveform on macro- and micro-
615 scale responses of ballast bed characterized in individual cycle: a numerical study. *Railw Eng*
616 *Science*. 2023;31:370–380.
- 617 [28] Luo Q, Fu H, Liu K, et al. Monitoring of train-induced responses at asphalt support layer of a
618 high-speed ballasted track. *Construction and Building Materials*. 2021;298:123909.
- 619 [29] Zhao W, Qiang W, Yang F, et al. Data-driven ballast layer degradation identification and
620 maintenance decision based on track geometry irregularities. *International Journal of Rail*
621 *Transportation*. 2023; 1–23.
- 622 [30] Cai X, Zhang Q, Wang Q, et al. Effects of the subgrade differential arch on damage
623 characteristics of CRTS III slab track and vehicle dynamic response. *Construction and Building*
624 *Materials*. 2022;327:126982.
- 625 [31] Liu H, Luo Q, Wang T, et al. Staged embankment construction in geotechnical centrifuges.
626 *Geotech Test J*. 2023;47:20220274.
- 627 [32] Liu H, Luo Q, El Naggar MH, et al. Centrifuge modeling of stability of embankment on soft
628 soil improved by rigid columns. *J Geotech Geoenviron Eng*. 2023;149:04023069.
- 629 [33] Gao M, Xu X, He R, et al. Vibration of subgrade and evaluation of derailment coefficient of
630 train under combined earthquake- moving train load. *Soils and Foundations*. 2021;61:386–400.
- 631 [34] Sadrekarimi A. Gravity Retaining Walls: Reinvented. 6th International Conference on
632 Earthquake Geotechnical Engineering. New Zealand; 2015. p. 9.
- 633 [35] FLAC3D 7.0 Documentation. Minneapolis: Itasca Consulting Group, Inc.; 2019.

- 634 [36] Friedman JH. Multivariate adaptive regression splines. *The Annals of Statistics*. 1991;19:1–141.
- 635 [37] Ren J, Deng S, Zhang K, et al. Design theories and maintenance technologies of slab tracks for
636 high-speed railways in China: a review. *Transportation Safety and Environment*.
637 2021;3:tdab024.
- 638 [38] Wang F, Qi J, Du J. Dynamic deformation analysis method and reliability on the subgrade
639 surface of the high-speed ballast track. *Journal of Safety and Environment*. 2016;16:144–149.
640 (in Chinese)
- 641 [39] Liu G, Luo Q, Zhang L, et al. Analysis on the dynamic stress characteristics of the unballsted
642 track subgrade under train loading. *Journal of the China Railway Society*. 2013;35:86–93. (in
643 Chinese)
- 644 [40] Luo Q, Zhang R, Xie H, et al. Structural analysis and key parameter of ballastless track subgrade
645 for 400 km/h high speed railway. *China Railway Science*. 2020;41:34–44. (in Chinese)
- 646 [41] Poulos HG, Davis EH. *Elastic solutions for soil and rock mechanics*. New York: Wiley; 1974.
- 647 [42] Wang T, Luo Q, Liu J, et al. Method for slab track substructure design at a speed of 400 km/h.
648 *Transportation Geotechnics*. 2020;24:100391.
- 649 [43] Vucetic M. Cyclic threshold shear strains in soils. *Journal of Geotechnical Engineering*.
650 1994;120:2208–2228.
- 651 [44] National Railway Administration of People’s Republic of China. Code for design of railway
652 earth structure. Beijing: China Railway Publishing House; 2016. Standard No. TB 10001-2016.
653 (in Chinese)
- 654 [45] Department of Housing and Urban-Rural Development of Liaoning Province. Technical Code
655 for Building Foundation. Shenyang: Liaoning Science and Technology Publishing House; 2015.
656 Standard No. DB21/T 907-2015. (in Chinese)
- 657 [46] Jaky J. The coefficient of earth pressure at rest. *Journal of the Society of Hungarian Architects
658 and Engineers*. 1944;78:355–358.
- 659 [47] Tschebotarioff G P. *Soil mechanics foundations and earth structures*. New York: McGraw-Hill;
660 1951.
- 661 [48] Lv W, Luo Q, Liu G, et al. Structural analysis and design method for subgrade bed of heavy
662 haul railway. *Journal of the China Railway Society*. 2016;38:74–81. (in Chinese)
- 663 [49] Bian X, Jiang H, Cheng C, et al. Full-scale model testing on a ballastless high-speed railway
664 under simulated train moving loads. *Soil Dynamics and Earthquake Engineering*. 2014;66:368–
665 384.

- 666 [50] Zhang WG, Goh ATC. Multivariate adaptive regression splines for analysis of geotechnical
667 engineering systems. *Computers and Geotechnics*. 2013;48:82–95.
- 668 [51] Zhang W, Goh ATC. Multivariate adaptive regression splines and neural network models for
669 prediction of pile drivability. *Geoscience Frontiers*. 2016;7:45–52.
- 670 [52] Zhang WG, Li HR, Wu CZ, et al. Soft computing approach for prediction of surface settlement
671 induced by earth pressure balance shield tunneling. *Underground Space*. 2021;6:353–363.
- 672 [53] Zhe L, Meizhen A, Linhou B, et al. Correlation analysis on telemetry data of manned spacecraft.
673 2018 Chinese Control And Decision Conference (CCDC). Shenyang: IEEE; 2018. p. 377–380.